

Supporting Information

Nawroth et al. 10.1073/pnas.1706926114

Animal Husbandry. Juvenile *E. scolopes* were obtained immediately after hatching from breeding colonies maintained in artificial seawater (ASW), as described previously (53). Between hatching and the start of experimental procedures, the hatching squid were kept individually in 5 mL of filter-sterilized ASW.

Bacterial Culture. GFP or RFP plasmid carrying *V. fischeri* wild-type strain ES114 was grown at 25 °C in tryptone-enriched ASW medium to the midlogarithmic phase to ensure bacterial motility. Cell density was estimated using optical density (OD) at 600 nm.

Particle and Bacteria Capture at the Ciliated Surface. Squid were placed individually in 5 mL of filter-sterilized ASW previously exposed to adult, colonized animals and hence containing mucus-release-stimulating bacterial peptidoglycan (PGN) (27) but no bacteria. *V. fischeri* and fluorescent polystyrene beads with 1- μm or 4- μm diameter (FluoSpheres Polystyrene Microspheres; Invitrogen) were added at equal concentrations and at a total concentration of 10^6 units/mL. After 100 min of exposure, the animals were imaged using confocal microscopy to determine the number of bacteria or beads attached to the ciliated surfaces of the light organ. Only intact and beating ciliated fields were included in the analysis.

Statistical Analysis of Particle Capture. Capture data of particles were tested for the null hypothesis that the datasets were drawn from continuous distributions with equal medians, against the alternative hypothesis that there was an increase in the median capture rate for smaller particles. We conducted a one-sided, non-parametric statistical test (Wilcoxon rank sum test) at a 5% significance level, using Matlab (MATLAB, The MathWorks, Inc.).

Confocal Imaging. For preparation, the animals were rinsed in ASW and incubated for 10 min with 10 $\mu\text{g}/\text{mL}$ fluorescently labeled wheat-germ agglutinin (WGA AlexaFluor 633; Molecular Probes). This lectin specifically binds to *N*-acetylneuraminic acid (sialic acid) residues present in the mucus lining of mucociliary surfaces (27). After staining, the squid were rinsed in ASW and anesthetized in 2% (vol/vol) ethanol in ASW. The animals were placed into a depression well slide with their abdominal side upward, and a window was cut into the mantle and funnel to expose the underlying ciliated surface. The preparation was viewed by a Zeiss LSM 510 or 710 confocal microscope.

Flow Visualization and Analysis. Unless indicated otherwise, for quantitative flow analysis, yellow-green fluorescent polystyrene microbeads (ex/em 505/515 nm; 1 μm and 4 μm diameter; Invitrogen) or GFP-expressing *V. fischeri* were added to the bath to serve as flow tracers. We verified that the particles are faithful tracers of the flow field and do not themselves alter the flow field by computing the particle Stokes number *St*. If $St \ll 0.1$, tracing accuracy errors are below 1% (54). Here, the Stokes number is defined as $St = t_p/t_f$, where t_p is the characteristic lag time of the particle's response to a change in fluid velocity (relaxation time), and t_f is the time of the fastest fluctuation of the flow field. For a spherical particle, t_p is given by $t_p = \rho_p d^2 / (18\mu)$, where $\rho_p = 1.05 \text{ g}/\text{cm}^3$ is the density of the polystyrene particles, $\mu = 1.08 \times 10^{-3} \text{ Pa}\cdot\text{s}$ is the dynamic viscosity of seawater at 20 °C, and d is the diameter of the particle. For the cilia-generated flow field, we define t_f as the duration of one ciliary beat cycle; i.e., $t_f = 0.1 \text{ s}$ at the 10-Hz beat rate observed in the squid cilia system. For the two particle diameters $d = 1 \mu\text{m}$ and $d = 4 \mu\text{m}$, we get $St = 0.54 \times 10^{-6}$ and $St = 8.6 \times 10^{-6}$, respec-

tively, indicating that the particles faithfully trace the flow as their response time is much faster than the fastest changes in the flow field.

For flow visualization, we used a portable laser with 473-nm wavelength (Aquarius Pro; Laserglow Technologies) diverged into a plane through a plano-concave cylindrical lens (focal length $f = -4$; Thorlabs). The laser was used to illuminate an ~ 0.5 -mm-thick 2D cross-section of the flow. The preparation was imaged under a dissection scope equipped with a high-definition camcorder (Sony HDR-CX560) and an optical 515-nm long-pass filter (Thorlabs). Particle traces were visualized by computing the SD of each pixel's brightness over all movie frames, using ImageJ (55). Individual particles were tracked using the ImageJ-Fiji plugin TrackMate (56) to measure velocities. Digital particle image velocimetry (DPIV) was performed using the Matlab-based software package PIVlab to compute average flow fields and streamlines from the particle displacements (57).

For ex vivo visualization and analysis of the ciliary currents, the light organ was excised and placed in ASW with suspended bacteria or microbeads. Video recordings of *V. fischeri* were taken at lower magnification than for particles because the GFP-fluorescent bacteria emit less light than light-scattering particles, hence limiting spatial resolution and accuracy of the tracked trajectories. For qualitative analysis of the flow, the ink sac embedded in the light organ was pierced using a microinjection needle, allowing the escaped ink to form a streakline that visualizes the oscillating nature of the flow field generated by metachronal ciliary beat (34) (Fig. 4A). Particle motions in the sheltered compartment were analyzed using mean-square displacement (MSD) analysis of the particle trajectories in 2D with the Matlab-class msdalyzer (58).

For in vivo visualization and analysis of the ciliary currents, the animals were prepared and imaged with confocal microscopy as described above. Fluorescent particles or bacteria were added to the preparation at a final concentration of 10^6 – 10^7 units/mL. Only intact and fully beating ciliated fields were included in the analysis. Particle or *V. fischeri* transport was imaged using time-lapse recording to reveal flow fields and particle accumulation.

For measuring in vivo inhalation flow, the intact and nonanesthetized animals were placed ventral side up in a plastic dish containing ASW with 10^7 fluorescent particles/mL with 1 μm and 4 μm diameter. We confirmed that the animals in- and exhaled particles of both sizes indiscriminately (Movie S1). Data from individually tracked particles and the DPIV-derived flow field of the funnel were used to estimate the Reynolds number, i.e., $Re = UD/\nu < 1$, where maximal flow velocity $U = 0.5 \text{ mm}/\text{s}$, exit nozzle diameter $D = 0.35 \text{ mm}$, and kinematic viscosity $\nu = 1 \text{ mm}^2/\text{s}$.

Model of Particle Capture by Direct Interception. We first assessed which of the common mechanisms underlying the capture of nonmoving particles at filter feeding structures would be most effective for the capture of microparticles at the squid appendages. These mechanisms include direct interception, inertial impaction, diffusion, and gravitational deposition of particles, and their relative importance in a given system can be assessed by computing previously described nondimensional indexes (5). Using these indexes, we estimated the relative contribution of each mechanism to the capture of relevant particle types from the mantle-driven flow (26). Here, we assume the following conditions: Temperature $T = 20 \text{ }^\circ\text{C}$, density of seawater $\rho_s = 1.025 \text{ g}/\text{cm}^3$, velocity of mantle-driven flow

$V = 100 \times 10^{-6}$ m/s, appendage diameter $D_c = 90 \times 10^{-6}$ m, and dynamic viscosity of seawater $\mu = 1.08 \times 10^{-3}$ Pa·s. We determined a dominant role of direct interception by computing the ratio of the direct interception index to the other indexes; specifically, we found the direct interception mechanism to be at least one order of magnitude more effective compared with any other mechanism. Table S1 lists the results, where N_I is the index of inertial impaction, N_R is the index of direct interception, N_G is the index of gravitational deposition, and N_M is the index of diffusional deposition.

Based on these results, we focused on estimating the effect of direct interception and ignored the other previously described capture mechanisms. The theoretical capture rate of particles by direct interception from the mantle-driven flow at the ciliated appendage was estimated by adapting a computational fluid dynamic (CFD) model for aquatic filter feeders (25). Briefly, the model predicts the capture rate of suspended particles by a cylindrical structure in a uniform flow. This model is valid for low to intermediate Reynolds numbers at the cylindrical structure, i.e., $Re_c < 50$, with $Re = UD_c/\nu$, where D_c is the diameter of the cylinder, U is the free-stream velocity, and ν is the kinematic viscosity of the fluid. Here, $Re_c \approx 0.01$, given a kinematic viscosity of water at 20 °C of $\nu = 1 \text{ mm}^2/\text{s}$ and the empirical measurements of ventilation flow $U_v = 0.1 \text{ mm/s}$ past the light organ and appendage diameter $D_c = 0.09 \text{ mm}$. For this Reynolds number regime, the model predicts that suspended particles with radius r_p will be intercepted at a per-second rate of $I_r = 2CU_v L\lambda$, with $\lambda = 0.218r_p^{1.938} + 0.117r_p^{1.923} Re_c$, where $C = 0.5 \times 10^3/\mu L$ denotes the number of particles/mm³ of fluid (corresponding to 500,000 particles/mL) and $L = 0.6 \text{ mm}$ is the total length of the two appendages per ciliated field. Total number of captured particles $I_T(t)$ over time t (in seconds) is estimated by $I_T(t) = I_r t$.

SEM. For SEM, animals were first anesthetized in 2% (vol/vol) ethanol in ASW. Before fixation, the mantle was cut open near the light organ to expose the light organ to the fixative agent. Then, the animals were rapidly fixed in 1% (wt/vol) osmium tetroxide in marine PBS (mPBS) (50 mM sodium phosphate, 0.45 M sodium chloride, pH 7.4). After 30 min of incubation, this was followed by fixation in 4% paraformaldehyde in mPBS. Fixation was allowed to proceed for 12–14 h at room temperature. Animals were then washed twice for 10 min in mPBS and dehydrated through an ethanol series (53). The samples were dried and gold sputter coated (Tousimis Samdri 780 critical point drier; SeeVac Auto conductavac IV), mounted on stubs, and viewed with a Hitachi S-570 LaB6 scanning electron microscope. In the digitized images, light-organ dimensions were measured using ImageJ.

High-Speed Video Recording. For high-speed imaging of ciliary beat, the animals were first anesthetized in a 2% (vol/vol) solution of ethanol in ASW. Then, the light organ was either imaged inside the animal through a window cut into the mantle (in vivo) or excised (ex vivo). Samples were placed in a plastic dish or depression slide with filtered ASW. For imaging of cilia–particle and cilia–bacteria interactions, microspheres or bacteria were added to a final concentration of 10^6 – 10^7 units/mL. The preparation was viewed using light microscopy (phase contrast, differential interference contrast, or fluorescent microscopy), paired with a high-definition camcorder (Sony HDR-CX560, image size $1,080 \times 1,920$ pixels) to record at 120 frames per second, or with a high-speed camera (Phantom v710, 1,000 fps, image size 800×600 pixels).

Kinematic Analysis of Ciliary Beat. Ciliary beat frequency (CBF) was determined from phase-contrast movie recordings of ciliary activity. An automated Matlab-based algorithm we have recently developed for in vitro analysis of ciliary beat (59) was used to

detect regions of interest (ROI), i.e., regions where ciliary activity is present. In these ROI, the intensity value of each pixel over time was bandwidth filtered, windowed, and analyzed using fast Fourier transform (FFT). The dominant frequency of the average power spectrum over all pixels in a given ROI corresponds to the CBF.

Kymograph analysis was performed using ImageJ. Beat kinematics of single cilia were determined by manually tracing individual cilia in subsequent frames of high-speed movie recordings of the ciliated surface. The traces were centered and overlaid to visualize the motion of the entire beat cycle.

Computational Model of the Vortical Flow Zone. We used a 2D continuum model to numerically study the ciliated appendages. Two cylinders of diameter D are fixed at a distance Δ apart, to mimic the frontal cross-section of the ciliated appendages. We prescribed tangential velocity boundary conditions on the surface of the cylinders (Fig. S6D). The velocity profile on the surface was chosen to match the distribution of cilia, their beat direction around the cylindrical appendage, and the empirical flow field, which consisted of two vortices and a sheltered zone. Since the long cilia beat in metachronal waves, we applied the boundary conditions at an effective diameter $D_{\text{eff}} = 0.95D$, which was roughly the midpoint of the highest and the lowest point on the wavy surface.

At zero Reynolds number, the fluid motion is governed by the Stokes equation $-\nabla p + \mu \nabla^2 \mathbf{u} = \mathbf{0}$ and the incompressible condition $\nabla \cdot \mathbf{u} = 0$, where p is the pressure field, \mathbf{u} is the fluid velocity field, and μ is the fluid viscosity. The boundary conditions are given by $\mathbf{u}|_{\infty} = U \mathbf{e}_y$ and $\mathbf{u}|_{\text{cylinder}} = u_t \mathbf{e}_\theta$, where u_t is the prescribed tangential velocity on the cylinder surface (Fig. S6E) and \mathbf{e}_θ is the unit tangent vector. In addition, we have a zero-force condition on the appendages. By symmetry, the net force in the x direction is automatically zero. The net force in the y direction is used to calculate the constant far-field velocity U . To obtain a nondimensional version of these equations, we used the length scale given by the cylinder diameter D and the timescale given by $D/\max(u_t)$. We numerically solved these equations using the regularized Stokeslets method. To this end, regularized Stokeslets were uniformly distributed along the cylinder surfaces. The fluid velocity at an arbitrary point \mathbf{x} in the fluid domain generated by N Stokeslets is $\mathbf{u}(\mathbf{x}) = \sum_{i=1}^N \mathbf{G}_s(\mathbf{x} - \mathbf{x}_i) \cdot \mathbf{f}_i$, where $\mathbf{G}_s(\mathbf{x} - \mathbf{x}_i) \cdot \mathbf{f}_i$ is the velocity field induced by a regularized Stokeslet of strength \mathbf{f}_i located at \mathbf{x}_i . We used the expression for $\mathbf{G}_s(\mathbf{x} - \mathbf{x}_i)$ given by Cortez (60). The resulting flow field is depicted in Fig. S6F.

To investigate how particles with different sizes move in the flow field generated by the ciliated appendages, we considered the model proposed in ref. 39. In the model, a particle of diameter d follows the streamline crossing its center when away from the cylinders. The particle velocity gets perturbed by $\Delta \mathbf{u} = \delta[(D + d)/2 - |\mathbf{x}_p - \mathbf{x}_c|] \frac{\mathbf{x}_p - \mathbf{x}_c}{|\mathbf{x}_p - \mathbf{x}_c|}$ when in contact with a cylinder, that is to say, when $(D + d)/2 - |\mathbf{x}_p - \mathbf{x}_c|$ is positive. Here, \mathbf{x}_p and \mathbf{x}_c are positions of the particle and cylinder, respectively, and δ is the strength of the perturbation due to the steric interaction between the particle and the cylinder. For small δ , the particle could penetrate the cylinder surface. Here, we used $\delta = 20$ and tested that the results are numerically robust at this value. We seeded the particles upstream uniformly with a spacing $d_s = 1/\rho_p$, where ρ_p is the density of the particles per unit length, along a seeding line of width 2Δ located at a distance $L_o = 5D$ from the center of the cylinders (to ensure that the particles were initially subject to a quasi-uniform flow). We released particles from their upstream positions and integrated their trajectories using an adaptive Runge–Kutta fourth- to fifth-order scheme with relative and absolute error tolerances of 10^{-16} . For a given separation distance Δ and particle size d , we calculated

the rate of particles captured between the cylinders. We considered the particles to be captured if the path lines of the particles cross the line connecting the centers of the cylinders (Fig. S6G). We defined the capture rate r_c as the ratio between the number c of captured particles and the total number of particles $2\Delta/d_s$; namely, $r_c = c/(2\Delta/d_s) = c/(2\rho_p\Delta)$. The results are depicted in Fig. 4H of the main text. Note that the actual value of ρ_p does not affect the results because the number of captured particles scales linearly with ρ_p . Also, the results are not sensitive to the initial position of particles as long as the particles are initially seeded sufficiently far upstream. We defined the critical diameter d_c as the largest diameter a particle can have and still reach the sheltered zone by following the flow field. We found that the compression of streamlines near the appendages results in particle streaming, where particles with diameter greater than d_c get diverted by the streamlines into the central outward jet (Fig. S6I). Particles of diameter equal to, or smaller than, d_c travel with the near-surface streamlines leading into the sheltered zone (Fig. S6H). The effect of D_{eff} on d_c is shown in Fig. S6J. Finally, we verified that the vortical flows and size-dependent particle capture are not universal to all possible boundary conditions by providing a counter example in Fig. S6 K–M. Clearly, for these made-up boundary conditions, no vortices were generated and no filtering by size was observed. This counter example neither proves uniqueness nor proves optimality of the boundary conditions (in other words, spatial distribution of cilia) that produce the counterrotating vortices. However, it confirms that the size-selective particle capture observed here is sensitive to the spatial distribution of cilia.

Computational Model of the Sheltered Zone. We considered a cluster of cilia whose base points are rooted on the surface ($x = 0$ plane) of a semiinfinite space $x = (0, \text{inf})$, with (x, y, z) being Cartesian coordinates. The length of each cilium is l and the spacing between the base points of neighboring cilia is D_y in the y direction and D_z in the z direction. We assumed that each cilium beats in the y direction and remains nondeformable as a rigid bar during the beating cycle. The angle between the cilium and the x axis was set to $\theta = \alpha \cos(2\pi\phi/T)$, where α is the beating amplitude and $\phi \in [0, T)$ is the phase of the cilium during the beating cycle. We considered the cilia carpet to be doubly periodic, and each periodic box had n_y cilia in the y direction and n_z cilia in the z direction. To compute the flow field generated by the cilia carpet, we approximated each cilium by a distribution of regularized Stokeslets along its centerline together with an “image” distribution to satisfy the no-slip boundary conditions at the base wall. The strength of each Stokeslet was computed by imposing the no-slip boundary conditions at the cilia, and the generated fluid velocity is $\mathbf{u}(\mathbf{x}, t) = \sum_{j=1}^{\infty} \sum_{k=1}^{\infty} \int_0^l \mathbf{G}(\mathbf{x}, \mathbf{x}_{jk}(s, t)) \cdot \mathbf{f}(\mathbf{x}_{jk}(s, t)) ds$, where j and k are indexes of the cilia in the y and the z direction, respectively. We used the expression of $\mathbf{G}(\mathbf{x}, \mathbf{x}_o)$ given by Ainley et al. (61). Due to the presence of the base wall, the infinite summation of the Stokeslets converges. Here, we approximated the infinite summations by using truncated sums $\sum_{j=1}^{J_{\text{max}}}$ and $\sum_{k=1}^{K_{\text{max}}}$. To avoid the edge effects, we considered only the results obtained for the middle periodic box.

To study the mixing effects of the short cilia with different phase coordination, we uniformly seeded the fluid domain near the cilia with passive tracers of two different colors in a 1:1 ratio. We considered two cases of initial seeding: horizontal strips and vertical strips. We computed the displacement field $\mathbf{d}(\mathbf{x}) = \int_0^T \mathbf{u}(\mathbf{x}(t), t) dt$ and used it as a discrete map $\mathbf{x}(t + T) = \mathbf{x}(t) + \mathbf{d}(\mathbf{x}(t))$ to study the long-term behaviors of the particle tracers. We adopted the mixing number $m = (\prod_{i=1}^N \min(|\mathbf{x}_i - \mathbf{x}_j|)^2)^{1/N}$, following Stone and Stone (36), where \mathbf{x}_i and \mathbf{x}_j are positions of tracer particles of different color and $j = 1, 2, \dots, N$, with N being the total number of same-color particles (Fig. S8 D–F and Fig. 5 E–H). Basically, we used the shortest distance between particles of different color as a measure for mixing, with a smaller mixing number indicating better mixing. We defined the mixing efficiency as $\eta_m = -\ln(m/m_0)/N_c$, where m_0 is the initial mixing number, and N_c is the number of cycles.

We considered three different cases of this model: (i) cilia beating in synchrony (SYNC); (ii) cilia beating in metachronal waves, in which case the phase difference between the neighboring cilia in the y direction is a constant, with $\Delta\phi \neq 0$ (META); and (iii) cilia beating at random phases (RAND), meaning that the initial phase of each cilium is taken from a uniform distribution ranging from 0 to T .

For these computations, each cilium was discretized into 20 regularized Stokeslets uniformly distributed along the centerline and the regularization parameter was chosen to be 0.05 to match a typical radius-to-length ratio. We prescribed the motion of each cilium as a rigid bar beating in the y direction, as noted at the beginning of this section. The beating amplitude was chosen to be $\alpha = 10^\circ$. We normalized length by the cilium length l and time by the beating cycle T . The distances between neighboring cilia were chosen to be $D_y = D_z = 0.5$. Each periodic box contained $n_y \times n_z = 8 \times 1$ cilia, and cilia with the same y values were considered to beat in phase. For the metachronal wave case, we used $\Delta\phi = T/8$ so that each periodic box contained one metachronal wave. Each beating cycle was discretized into 50 time steps and the particle tracer positions were integrated using a fourth-order Runge–Kutta scheme. For the random-phase case, 10 Monte Carlo simulations were performed to get a distribution of results.

Computational Model of Transport by Single Cilium. We compared the fluid transport generated by a single cilium with different beating patterns (Fig. S8 A–C). The beating pattern of a single cilium was studied by Eloy and Lauga (62), who found that for optimal transport the cilium exhibited a small curvature during the effective stroke and large curvature during the recovery stroke. Here, we used an asymmetric beating pattern adapted from the rabbit tracheal cilia (9), which exhibits a nearly straight effective stroke and a curly recovery stroke. The symmetric beating pattern was extracted from high-speed video recordings of the short cilia in the squid ciliated organ (Movie S2).

Using the regularized Stokeslet method with image distributions described in the previous section, we derived the flow velocity field for each of the two beating patterns. We further integrated the flow generated by the single cilium over one cycle to evaluate the transport efficacies of different beating patterns quantitatively.

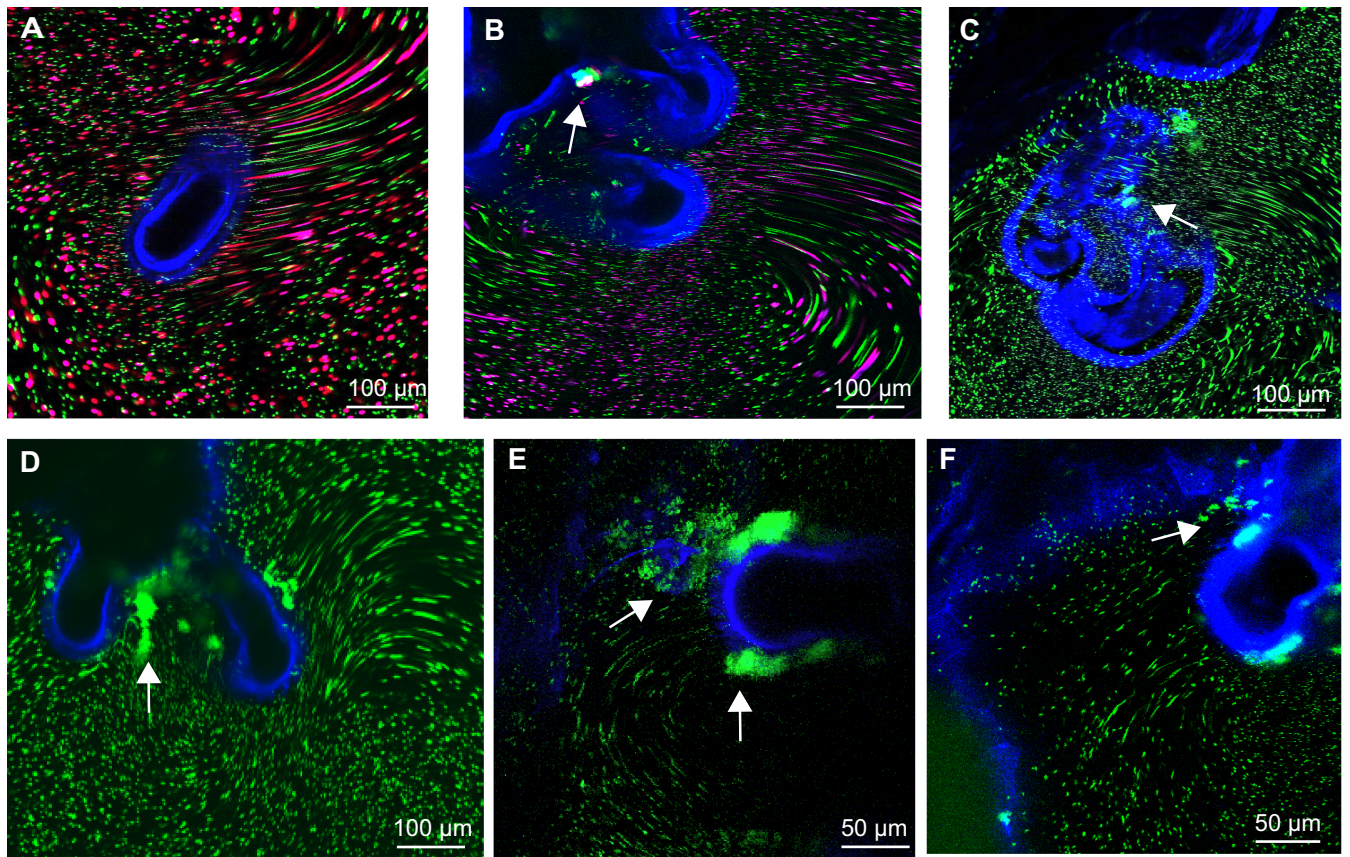


Fig. 55. Time-lapse confocal recordings confirm similar trajectories of particles and bacteria in light organs not excised from the mantle cavity. (A) Trajectories of 4- μm (red) and 1- μm (green) particles near the ciliated appendages. The prolonged-exposure streaklines indicate relatively rapid flow on the right side where the long cilia are located and relatively slow flow on the left side, toward the sheltered zone. (B) Vortical transport of these particles and their accumulation in the sheltered zone (arrows) between appendages, showing accumulation of 1- μm (green) particles at higher rates than the 4- μm particles, despite their lower statistical chance of capture by direct interception. (C and D) Vortical transport and accumulation in the sheltered zone (arrows) of 1- μm (green) particles. (E and F) Vortical transport and accumulation in the sheltered zone (arrows) of *V. fischeri* cells (green). Blue, mucus coating on the appendages in all images.

are labeled red. Comparing the fate of small particles (*Left*) (particle diameter $d = 1\%$ of appendage diameter D) and of large particles (*Right*) ($d = 15\% D$) shows that in this flow field, particle size has no effect on particle capture, demonstrating that applying a different tangential velocity profile from the one observed empirically (*C* and *D*) can lead to a nonvortical flow pattern with no particle sorting mechanism.

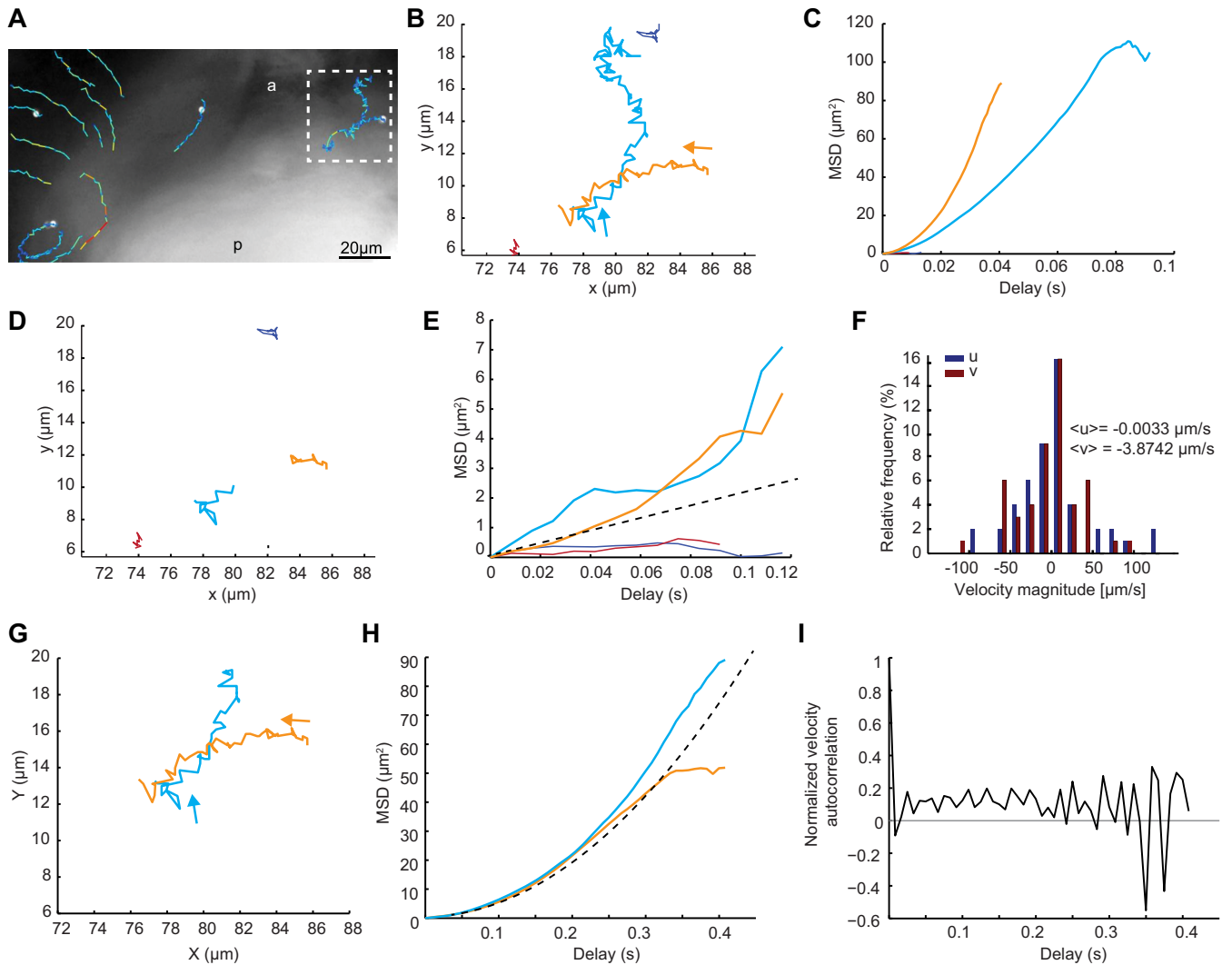


Fig. S7. Particle trajectories in sheltered zone reveal both diffusion-like and directional transport. (*A*) Particle trajectories in the fast-flowing regions covered by long cilia (*Left*) and the sheltered zone covered by short cilia (*Right*, white dashed rectangle). (*B*) Four particle trajectories recorded in the sheltered zone. Arrows indicate starting point and direction of the trajectories. (*C*) MSD analysis of the four trajectories shown in *B*. (*D*) The initial 100 ms of the four trajectories are used to analyze the contribution of diffusion. (*E*) The mean MSD (dashed line) of the first 100 ms is approximated by the linear trend $\text{MSD}(t) = 4Dt$, where $D \approx 7 \mu\text{m}^2/\text{s}$ is the diffusion coefficient. This coefficient is of comparable magnitude to the theoretical value of $D = 2 \mu\text{m}^2/\text{s}$ for a $1\text{-}\mu\text{m}$ tracer in water using the Stokes–Einstein equation (63). (*F*) Histogram of x and y velocity magnitudes during the first 100 ms. The diffusive behavior is further supported by a near-zero mean of these distributions. Mean values are $\langle u \rangle = -0.0033 \mu\text{m/s}$ and $\langle v \rangle = -3.8742 \mu\text{m/s}$. (*G*) The first 400 ms of the two long trajectories are used to analyze the contribution of convection. (*H*) The mean of the MSDs (dashed line) of the first 400 ms follows a parabolic trend approximated by $\text{MSD}(t) = 4Dt + U^2 t^2$, where $D \approx 4 \mu\text{m}^2/\text{s}$, and $U \approx 20 \mu\text{m/s}$ is the flow velocity, which is one order of magnitude smaller than the velocities reached in the neighboring, long-cilia-driven flow. (*I*) Mean autocorrelation of the first 400 ms shows similarity with a Dirac function, indicating that over time, directional transport cancels out.

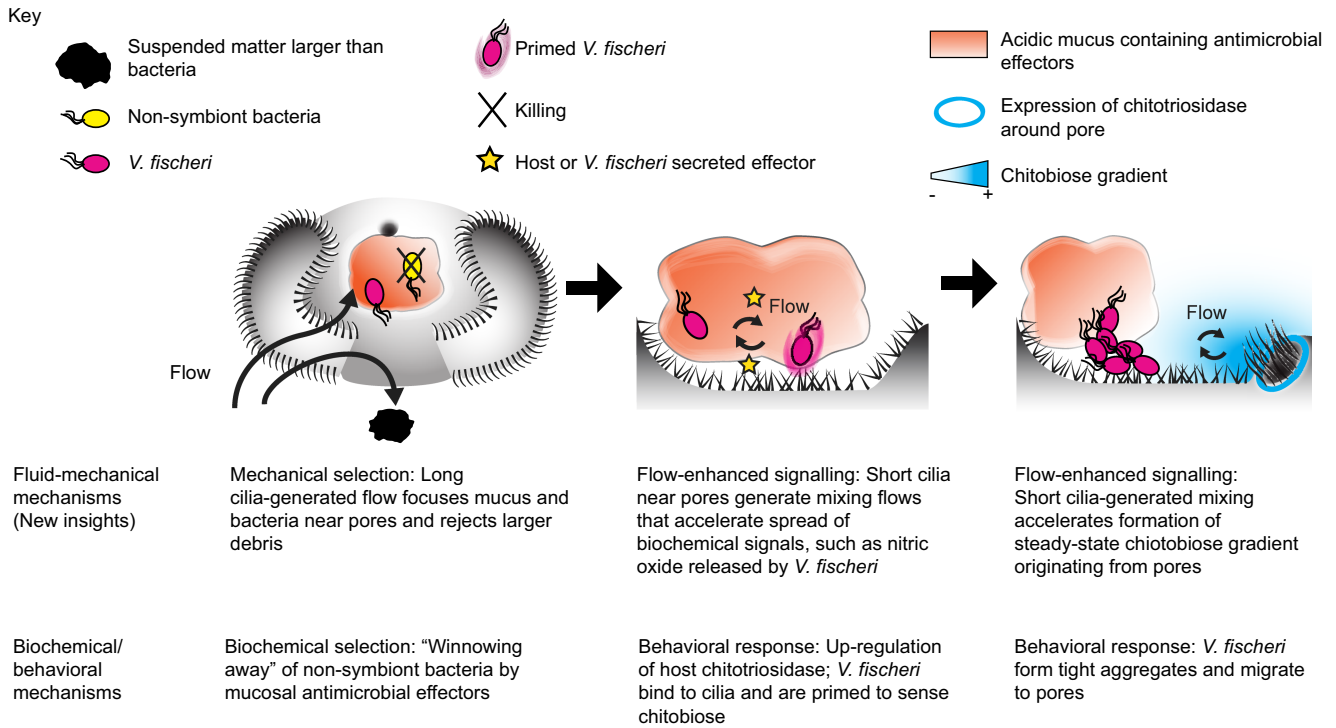
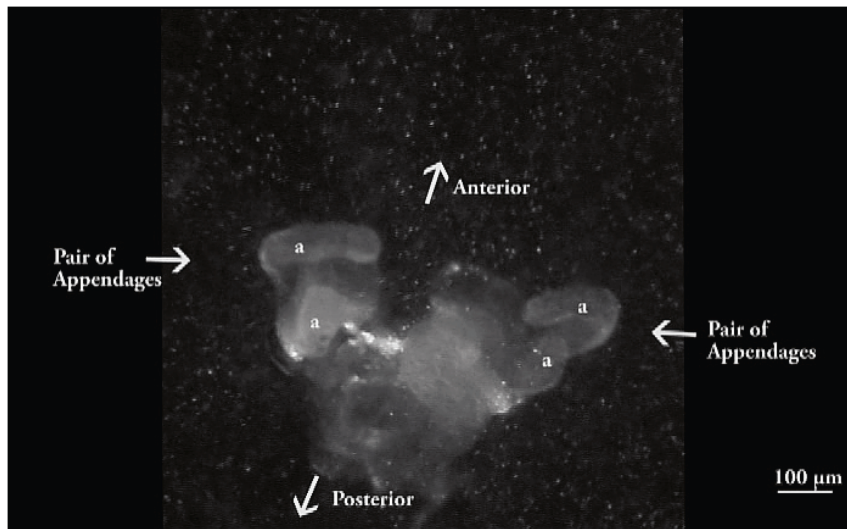


Fig. S9. Summary of findings in the context of symbiont–host association. The proposed fluid-mechanical mechanisms involved in symbiont-host association are proposed to occur in combination with known biochemical and behavioral mechanisms (refs. 18 and 19).

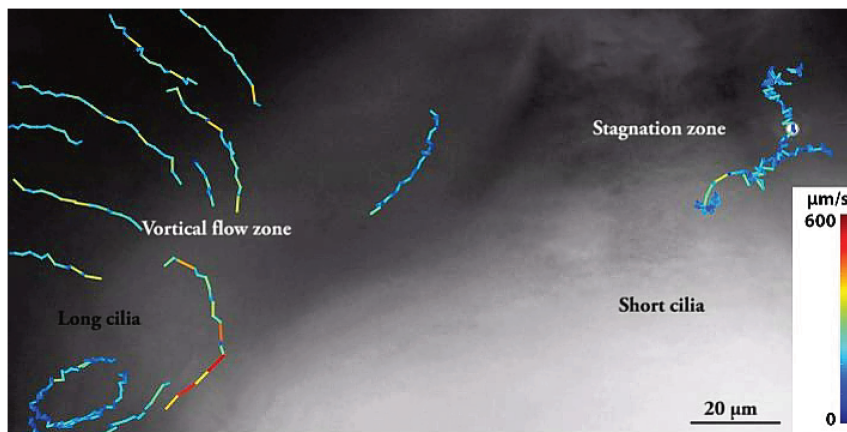
Table S1. Relative efficiency of possible mechanisms for capturing particles from mantle-driven flow (adapted from ref. 26)

| Particle type | Density, g/cm ³ | Diameter, μm | N_R/N_I | N_R/N_G | N_R/N_M |
|------------------|----------------------------|--------------|-------------------|-----------|-------------------|
| Bacterium | 1.075 | 1 | 3.9×10^6 | 44.1 | 0.3×10^3 |
| Phytoplankton | 1.095 | 5 | 0.6×10^6 | 6.3 | 6.3×10^3 |
| Polystyrene bead | 1.05 | 1 | 7.8×10^6 | 88.1 | 0.3×10^3 |
| Polystyrene bead | 1.05 | 4 | 1.9×10^6 | 22.0 | 4.0×10^3 |



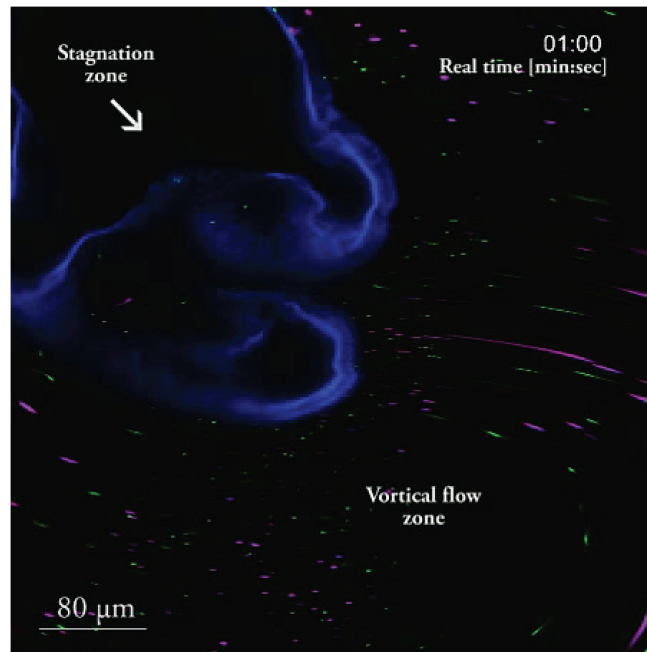
Movie S3. Cilia-generated flow field of the ciliated epithelium. Visualization of microparticle transport in both the ex vivo and the in vivo ciliated light organ shows that the majority of particles entrained into the long-ranging vortical flow zone are deflected from the surface whereas a small fraction of particles can enter and accumulate in the stagnation zone between the appendages.

[Movie S3](#)



Movie S4. The ciliated epithelium features two distinct microfluidic zones. Clip 1 is a close-up of the microparticle transport in the ex vivo light organ showing fast, directed transport in the vortical flow zone and, in contrast, slow, diffusion-like transport in the neighboring stagnation zone lined by short cilia. Clip 2 shows mucus and particles trapped in the stagnation zone being gently rocked by the motion of the short cilia.

[Movie S4](#)



Movie S5. In vivo recording of cilia-generated flow zones and size-biased particle capture. Confocal time-lapse recording of the in vivo ciliated surface (blue) shows distinct vortical flow and stagnation compartments, as well as preferential accumulation of 1- μm particles (green) compared with 4- μm particles (red) in the stagnation zone.

[Movie S5](#)



Movie S6. The ciliated surface appendage features circumferential ciliary beat. Cross-sectional view onto ciliated light-organ appendage shows the circumferential ciliary beat and the parting point at which beat direction reverses, creating a flow that passes the appendage left and right of the parting point.

[Movie S6](#)